








# Optimizing Photometric Redshift Training Sets I: Efficient Compression of the Galaxy Color–Redshift Relation with UMAP

FINIAN ASHMEAD <sup>1,2</sup> JEFFREY A. NEWMAN <sup>1,2</sup> BRETT H. ANDREWS <sup>1,2</sup> RACHEL BEZANSON <sup>1,2</sup>  
BIPRATEEP DEY <sup>3,4,5,6</sup> DANIEL C. MASTERS <sup>7</sup> AND S.A. STANFORD <sup>8</sup>

<sup>1</sup>*Department of Physics and Astronomy, University of Pittsburgh, Pittsburgh, PA 15260, USA*

<sup>2</sup>*Pittsburgh Particle Physics, Astrophysics, and Cosmology Center (PITT PACC), University of Pittsburgh, Pittsburgh, PA 15260, USA*

<sup>3</sup>*Department of Statistical Sciences, University of Toronto, Toronto, ON M5G 1Z5, Canada*

<sup>4</sup>*Canadian Institute for Theoretical Astrophysics (CITA), University of Toronto, Toronto, ON M5S 3H8*

<sup>5</sup>*Dunlap Institute for Astronomy & Astrophysics, University of Toronto, Toronto, ON M5S 3H4, Canada*

<sup>6</sup>*Vector Institute, Toronto, ON M5G 0C6, Canada*

<sup>7</sup>*Caltech/IPAC, 1200 E. California Blvd. Pasadena, CA 91125, USA*

<sup>8</sup>*Physics and Astronomy Department, University of California Davis, CA 95616*

## ABSTRACT

Spectroscopic datasets are essential for training and calibrating photometric redshift (photo- $z$ ) methods. However, spectroscopic redshifts (spec- $z$ 's) constitute a biased and sparse sampling of the photometric galaxy population, which creates difficulties for the common grid-based approach for mapping color to redshift using self-organizing maps (SOMs). Instead, we utilized the uniform manifold approximation and projection (UMAP) algorithm to compress a Rubin–Roman-like *ugrizyJH* color space into a thin and densely-sampled manifold. Crucially, the manifold varies continuously and monotonically in redshift and specific star formation rate in roughly orthogonal directions. Using  $\sim 110,000$  COSMOS2020 many-band photo- $z$ 's and  $\sim 15,000$  spec- $z$ 's as representative and non-representative samples, respectively, we trained and tested redshift estimation from a SOM (SOM- $z$ ) and from nearest neighbors in UMAP space (UMAP- $k$ NN- $z$ ). Compared to SOM- $z$ , UMAP- $k$ NN- $z$  exhibited smaller photo- $z$  scatter and fraction of outliers for the representative training set. When training with the highly biased spec- $z$  sample, UMAP- $k$ NN- $z$  maintained similar performance, but the outlier fraction for SOM- $z$  increased by nearly three times. The physically-meaningful trends across the UMAP manifold allow for accurate redshift regression even in regions of color space sparsely populated by spectroscopic objects, which comprise nearly 25% of the photometric sample. This suggests that representative, spectroscopically-anchored training sets can be produced by interpolating between spectroscopic sources at the UMAP coordinates of photometric objects, maximizing the performance of photo- $z$  algorithms.

**Keywords:** Redshift — Cosmology — Galaxy Evolution — Machine Learning — Dimensionality Reduction

## 1. INTRODUCTION

Photometric redshifts (photo- $z$ 's) are critical to extragalactic science. Cosmological measurements via weak lensing and large-scale structure are particularly dependent on photo- $z$ 's to accurately characterize redshift distributions for large samples of galaxies (Mandelbaum 2018). For upcoming experiments, characterization of

photo- $z$  distributions is expected to be a leading source of systematic uncertainty (The LSST Dark Energy Science Collaboration et al. 2018, Newman & Gruen 2022).

Photometric redshift techniques fall broadly into two categories, template-based and machine-learning-based, both of which rely on spectroscopic redshifts (spec- $z$ 's) in calibration or training data (Salvato et al. 2019). Both classes of techniques are limited by sparse sampling of color space, and the systematic differences in magnitude, color, and redshift distributions between photometric and spectroscopic samples. Machine-learning-

based techniques in particular make a strong assumption that the spec- $z$  training data is representative of the target sample to which the photo- $z$  algorithm will be applied, and deviation from this assumption limits their performance (Newman & Gruen 2022).

Real spectroscopic datasets deviate from being representative samples of larger photometric datasets for several reasons. Spectroscopic surveys are generally designed with cuts on the magnitude, color, or surface brightness of target galaxies in order to ensure high success rates within limited exposure time or target galaxies in a particular redshift range. This introduces selection effects into the spectroscopic dataset that will not reflect the distributions of galaxy properties in more inclusive photometric surveys. Spectroscopic datasets also include unintentional selection effects, resulting from non-uniform probabilities of obtaining a secure redshift measurement for different galaxy populations across redshifts, as well as unavoidable selection effects due to atmospheric absorption in certain wavelength ranges, most notably the infrared. These effects result broadly in higher-redshift objects and dimmer objects across redshifts being under-represented in spectroscopic datasets. For instance, Khostovan et al. (2025) found that spectroscopic observations in the COSMOS field have poor coverage of intermediate-mass quiescent galaxies and low-to-intermediate-mass “bursty” star-forming galaxies at  $z < 1$ , massive quiescent galaxies at  $z \sim 2$ , and massive star-forming galaxies at  $z > 3$ .

Deep spectroscopic datasets generally come from a limited area on the sky, with their redshift distributions reflecting the cosmic structure along that particular line of sight, which will not be representative of the general redshift distribution of galaxies. Different populations of galaxies also cluster differently, introducing further bias when these populations are not represented proportionally in the spectroscopic dataset (as is generally the case in practice). Furthermore, the limited sky area of these surveys entails limited volume at low redshift, making it difficult to obtain representative samples in this regime. Finally, even high-confidence spectroscopic redshift datasets contain a non-negligible fraction of incorrect redshifts, degrading photo- $z$  performance.

Photometric redshift techniques are fundamentally mappings of observed galaxy spectral energy distributions (SEDs) to redshift. There are many possible degeneracies in particular bands or colors, for example the Balmer/4000Å break at  $z \sim 0.3$  and the Lyman break at  $z \sim 3$  would both be observed as a steep rise in flux between the  $g$  and  $r$  bands. These degeneracies can often be lifted with the inclusion of measurements in additional bands, with the tradeoff that increasing

the dimensionality of the color space exponentially increases its volume, leading to sparse sampling by the data (McCullough et al. 2024). This is known as the curse of dimensionality, and makes interpolating in high-dimensional spaces difficult and unreliable.

Observed galaxy colors however, are highly correlated and occupy only a subset of the space, being largely driven by only two parameters, redshift and specific star formation rate (sSFR). With a proper application of dimensionality reduction, it should be possible to recover this structure. Self-organizing maps (SOMs; Kohonen 1982) have become a popular approach to embed higher-dimensional galaxy photometry into a two-dimensional grid and map the cells to redshift, sSFR, and other physical galaxy properties (e.g., Carrasco Kind & Brunner 2014, Masters et al. 2015, Hemmati et al. 2019, Khostovan et al. 2025).

The SOM algorithm assigns objects to cells on a regular grid, losing some information to binning, while also inhibiting it from capturing intrinsic structure in the data that may be better represented using a different geometry. A SOM can be used to assign redshifts to objects based on the known redshifts of sources in the same cell. However, major discontinuities in the redshifts of objects occupying adjacent cells make it infeasible to interpolate reliably across the map for objects in cells without any known redshifts. Here, we explore alleviating these drawbacks using the uniform manifold approximation and projection algorithm (UMAP, McInnes et al. 2018), which has the advantage of projecting all of the data into a *continuous* low-dimensional space and is designed to capture both local and global structure in datasets. By predicting redshifts from the low-dimensional coordinates and quantifying the performance with common photo- $z$  evaluation metrics, we quantify the reliability of the color-redshift mapping in these compressed spaces.

In Section 2, we describe the data used in this analysis. In Section 3, we detail our creation of SOM and UMAP embeddings of our input data, and describe the resulting spaces qualitatively. In Section 4, we describe our quantitative assessment of the color-redshift mappings provided by the SOM and UMAP embeddings, comprising their use as redshift estimators and the metrics used to evaluate their performance. In Section 5, we comment on these results and the future direction of this work.

## 2. DATA

In our analysis we used photometry and template-based, many-band photometric estimates of redshift and sSFR from the Farmer version of the COSMOS2020 cat-

alog (Weaver et al. 2022) and spectroscopic redshifts from the COSMOS Spectroscopic Redshift Compilation (Khostovan et al. 2025; hereafter CSRC).

### 2.1. COSMOS2020

For the COSMOS2020 catalog, we removed areas of the field with partial coverage or unreliable photometry, which we implemented by requiring `FLAG_COMBINED=0`, reducing the sample from 964,506 sources to 746,976. We corrected for Milky Way extinction according to the dust map of Schlegel et al. (1998). We also corrected for the systematic photometric offsets derived from LePHARE based on COSMOS spectroscopic sources, following the COSMOS2020 example Jupyter notebook (Blanquez et al. 2023).

The COSMOS2020 catalog features estimates of galaxy properties (e.g., redshift, sSFR) calculated using two different SED template-fitting codes, EAZY (Brammer et al. 2008) and LePHARE (Arnouts et al. 1999, Ilbert et al. 2006). LePHARE finds the combination of template and redshift that minimizes the chi-squared with respect to the observed photometry, and in the case of COSMOS2020 was implemented in the configuration used by Ilbert et al. (2013). EAZY is implemented similarly, with differences in the template library and fitting method used. We adopted the LePHARE redshift estimates as they had a lower outlier rate than EAZY when evaluating with spec- $z$ 's (using the metrics defined in Section 4.2).

The LePHARE many-band photometric redshifts in COSMOS2020 (LePHARE- $z$ 's) have the advantage of being based on up to 30 broad, medium, and narrow bands spanning the UV to IR wavelengths (with as few as 17 bands being used for objects in our sample). These photo- $z$ 's have the utility of being representative of the photometric sample, while being more accurate than broadband-only photo- $z$ 's. Although they are relatively reliable, they do have a significant outlier rate compared to spectroscopic data, particularly in the faint regime, approaching 4% for objects with  $24.25 < i < 24.5$ . Nonetheless, for the purposes of our quantitative analysis of SOM- and UMAP-based redshift estimation, we treat the LePHARE- $z$ 's as true.

We applied three additional cuts to the COSMOS2020 catalog. We removed sources with LePHARE redshifts  $z_{\text{LePHARE}} < 0.01$  due to their significant likelihood of being misclassified stars, bringing the dataset down to 709,024 sources. We also restricted our analysis to sources with both  $i < 24.5$  and  $H < 24.8$ , comparable to the expected magnitude limits for early LSST or Roman weak lensing analyses, leaving us with 121,791. These cuts also helped to eliminate objects that may have

large photometric uncertainties and potentially poorly-constrained photometric redshifts.

Throughout this paper, we applied dimensionality reduction methods to a seven-dimensional parameter space consisting of the  $u - g$ ,  $g - r$ ,  $r - i$ ,  $i - z$ ,  $z - y$ ,  $y - J$ , and  $J - H$  colors of the objects. This approximates the colors between successive bands that will be available by combining the medium tier of the Roman High-Latitude Wide Area Survey (HLWAS) with the Rubin Legacy Survey of Space and Time (LSST) (Zasowski et al. 2025). We utilized the combined  $u$ -band photometry presented in COSMOS2020 (Sawicki et al. 2019, Weaver et al. 2022). The *grizy* data in COSMOS2020 were taken from the second data release of the Hyper Suprime-Cam Subaru Strategic Program (Aihara et al. 2019). The  $J$  and  $H$  near-infrared data in COSMOS2020 were taken from the fourth data release of the UltraVISTA survey (McCracken et al. 2012). We tested alternate sets of eight colors (adding  $J - K_s$ ) and ten colors (adding the Spitzer IRAC-based colors  $K_s - Ch1$  and  $Ch1 - Ch2$ ), obtaining results similar or worse to those based on the seven-color space.

In addition to the cuts described above, we removed all sources missing measurements in any of the photometric bands defining the input color space, or LePHARE photo- $z$  or sSFR. In the end, our sample includes 112,409 sources.

### 2.2. COSMOS Spectroscopic Redshift Compilation

The COSMOS Spectroscopic Redshift Compilation (CSRC, Khostovan et al. 2025) compiled  $\sim 165,000$  spec- $z$ 's of  $\sim 98,000$  unique objects taken in the COSMOS field over the course of  $\sim 20$  years in 108 observing programs. To utilize CSRC spec- $z$ 's we performed a spatial cross-match to our COSMOS2020 photometric data, considering the nearest COSMOS2020 source (with a maximum separation of  $0.5''$ ) as the counterpart of a CSRC object. We obtained 35,346 matches, with a large fraction of unmatched CSRC objects being in regions outside of the formal COSMOS2020 catalog area or in masked regions within it.

The CSRC compiled redshifts from observing programs using various quality flagging systems, so the authors normalized confidence levels (CL) and quality flags ( $Q_f$ ) based on the popular 0 – 4 scheme for all CSRC redshifts to create a consistent scale. From our cross-matches we selected sources with  $CL > 95$ , corresponding to  $Q_f = 4$  or a *very reliable redshift*, obtaining a sample of 14,499 objects (hereafter referred to as the spec- $z$   $CL > 95$  sample).

In Figure 1, we show density-normalized histograms illustrating the differences in the distributions in red-

shift, color, and magnitude between the spectroscopic and photometric samples. It is notable that even in this case where the observations target the same field, and therefore trace the same line of sight through cosmic structure, the spectroscopically-observed objects are still clearly not representative of the larger photometric sample. For data taken from different fields the existing discrepancies would be much starker, particularly in the case of the fluctuations in redshift distributions.

### 3. DIMENSIONALITY REDUCTION METHODS

SOM-based approaches to mapping the high-dimensional space of galaxy colors to physical properties and redshift are quite popular, but are limited by the discrete grid and enforced topology such that interpolation across cells is not robust. By using UMAP as an alternative approach to compressing the high-dimensional space of galaxy colors, we seek to overcome these limitations that hinder redshift prediction.

#### 3.1. SOM

We implemented SOM using the `minisom` Python package (Vettigli 2018). For a given dataset, one of the most critical choices is that of the SOM size; a higher cell count will capture the structure of the input space in greater detail, but the cells will be increasingly sparsely populated. The overall shape of the SOM and its constituent cells can also be customized (see Carrasco Kind & Brunner 2014), but for the purposes of this investigation we adopt the convention of using rectangular SOM embeddings with a  $1 \times 2$  aspect ratio consisting of rectangular cells as in, e.g., Masters et al. (2015).

In our testing of the accuracy of redshift predictions based on position in SOM or UMAP coordinates, we split our dataset into training and test samples, and estimated the redshifts of the test sources based on the training sources, comparing to the LePHARE photo- $z$  for evaluation. In one test, the 14,499 objects with high-confidence spec- $z$ 's were used as the training set, while in the other an equivalent number of random objects with LePHARE redshifts comprised the training sample. For this application, sparsely populated SOM cells are particularly problematic, as for increasing cell count an increasing number of test sources will be placed in cells with no training sources which could be used to assign a redshift.

We generated rectangular SOM embeddings for various total cell counts between 128 ( $8 \times 16$ ) and 11,250 ( $75 \times 150$ ), deciding on the  $50 \times 100$  grid as providing the best balance of a detailed representation of the color space with a minimal number of unoccupied cells. Similarly, we chose 0.8 and 1, respectively, for the learn-

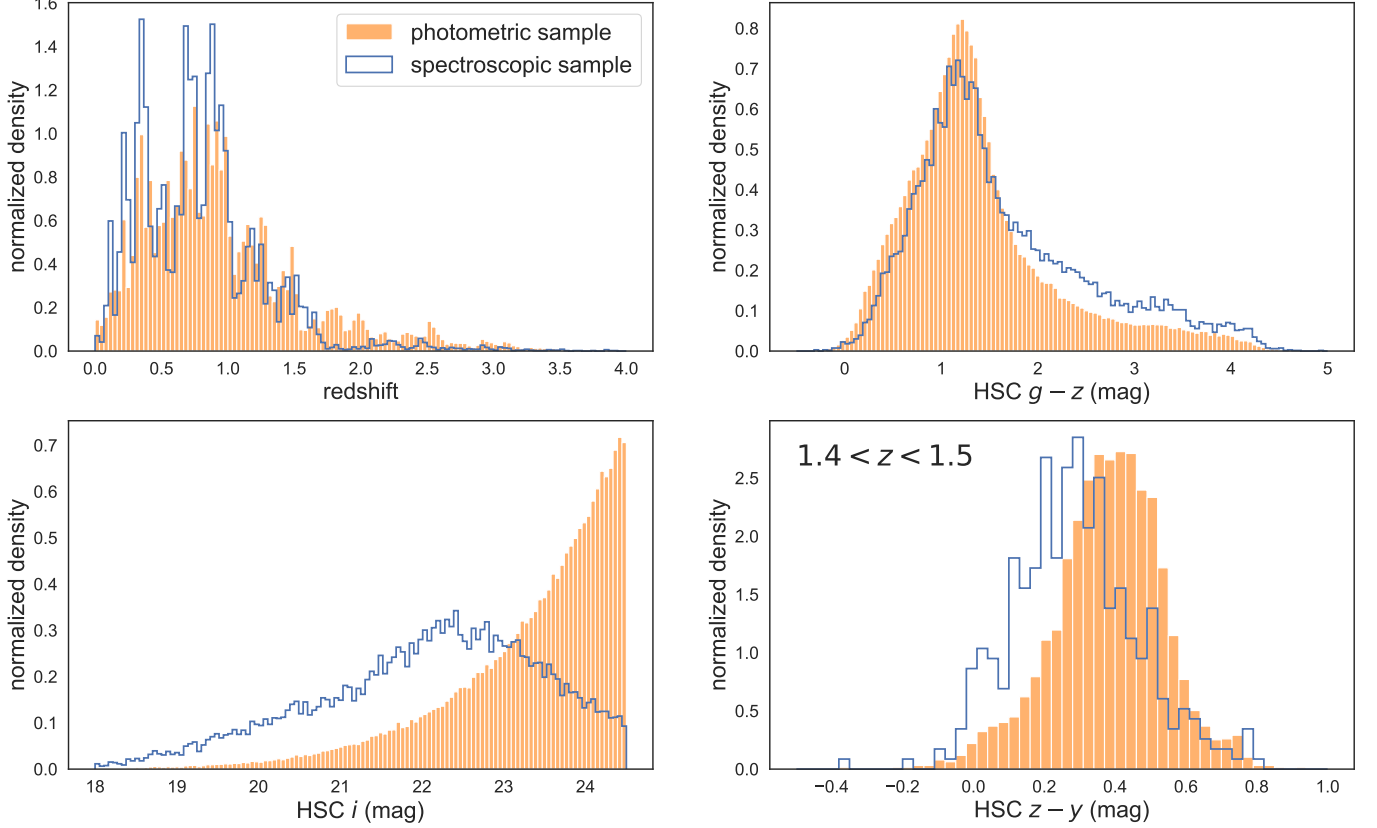
ing rate and sigma hyperparameters, as this combination yielded an embedding with all 50,000 cells occupied. These choices are explained in greater detail in Appendix A. To train to convergence, we used two million learning epochs.

Figure 2 shows our SOM embedding of *ugrizyJH* color space, color-coded by cell galaxy count, median redshift, and sSFR in the left, center, and right columns, respectively. The top row shows the full photometric sample of 112,409 galaxies, while the middle and bottom rows are populated with 14,499 galaxies each. The middle row corresponds to a random subsample of the full dataset, while the bottom row corresponds to the subset of galaxies with high-confidence spec- $z$ 's. Both redshift and sSFR are generally well-organized within particular neighborhoods of SOM cells, but there are often strong discontinuities in both quantities across adjacent cells at the borders of these neighborhoods. These discontinuities indicate that SOM offers a less reliable mapping between the observable colors and the physical parameters driving them, and introduces problems for tasks like redshift interpolation. Comparing the lower two rows illustrates the incomplete and biased sampling of the color space by spectroscopic datasets. While the gaps in the random subsample are smaller and more dispersed, the spectroscopic sample lacks representation in large, correlated regions of the color space.

#### 3.2. UMAP

While SOMs implement a discrete, (generally) rectangular binning of the data into a grid, UMAP is more flexible and projects each data point individually into a lower-dimensional space. The UMAP algorithm assumes the existence of a manifold on which the data is uniformly distributed and locally connected, and is optimized to preserve the topological structure of this manifold (McInnes et al. 2018).

UMAP constructs a weighted  $k$ -neighbor graph of the data that represents the data's connectivity, in which each point corresponds to a vertex and each vertex has edges to its  $k$  nearest neighbors. In this graph, each point will have an edge weight of one for its nearest neighbor, indicating they are connected, with exponentially decreasing edge weights out to the  $k$ -th neighbor, indicating progressively lower probability of more distant points being connected. The edge with weight one ensures each point is connected to at least one other, while the decreasing edge weights to the  $k$ -th neighbor allow data with non-uniform density to be handled consistently. UMAP determines the low-dimensional embedding by optimizing a weighted graph of the output space for similarity to that of the input space, with the



**Figure 1.** The distributions of our photometric (orange) and spectroscopic (spec- $z$  CL > 95; blue) samples in redshift (upper left),  $g - z$  color (all redshifts; upper right),  $i$ -band magnitude (lower left), and  $z - y$  color for objects at redshifts  $1.4 < z < 1.5$  (lower right). Higher redshifts, particularly at  $z > 1.5$ , are underrepresented in the spectroscopic sample, as are objects fainter than  $i \sim 23$ . The  $g - z$  color distribution is redder overall for the spectroscopic sample, while the  $z - y$  color at  $1.4 < z < 1.5$  is systematically bluer for the spectroscopic sample. In the case of the  $g - z$  distribution, the apparent overabundance of spectroscopic sources at  $g - z \gtrsim 1.5$  reflects redder galaxies at  $z < 1$ , while in the case of the  $z - y$  distribution for  $1.4 < z < 1.5$ , the bluer colors of the spectroscopic sample reflect a preference for star forming galaxies. Offset color distributions at fixed redshift such as that shown in the lower right will bias color–redshift mappings based on non-representative spectroscopic samples. The spectroscopic sample’s biased coverage of color space can also be seen in the bottom row of Figure 2.

difference that in this case the weights are a function of absolute distance in the low-dimensional space rather than the distance to the  $k$ -th nearest neighbor.

The critical hyperparameters when using UMAP are therefore the number of neighbors used to construct the graph (`n_neighbors`), the desired minimum distance between points in the output space (`min_dist`), and the distance metric used in the input space (e.g., Euclidean, Manhattan, or cosine; the Euclidean metric is used in the output space). Another important choice is whether to rescale the input data such that each input dimension has similar dynamic range.

We implemented UMAP using the `umap-learn` Python package. As with SOM, we tested a variety of combinations of hyperparameter choices, including values of `n_neighbors` from 10 to 200 and values of `min_dist` from 0.00 to 0.20. We ultimately obtained the best result using non-rescaled data, the Manhattan

distance metric in the input space, and hyperparameters `n_neighbors` = 80 and `min_dist` = 0.00. These choices are explained in greater detail in Appendix B.

In Figures 3 and 4 we show our UMAP embedding of *ugrizyJH* color space populated with the 112,409 galaxies in the photometric dataset and the 14,499 galaxies in the spectroscopic dataset, respectively, corresponding to the datasets in the top and bottom rows of Figure 2. We recovered a thin manifold embedded in three dimensions with continuous, monotonic, and roughly orthogonal variation in redshift and sSFR. Although the spectroscopic sources shown in Figure 4 provide a relatively sparse sampling of the space, the well-behaved and physically-meaningful organization of the manifold mitigates the impact of this. Due to its embedding into a continuous space and its monotonic variation in redshift, UMAP avoids the issue of gaps and discontinuities



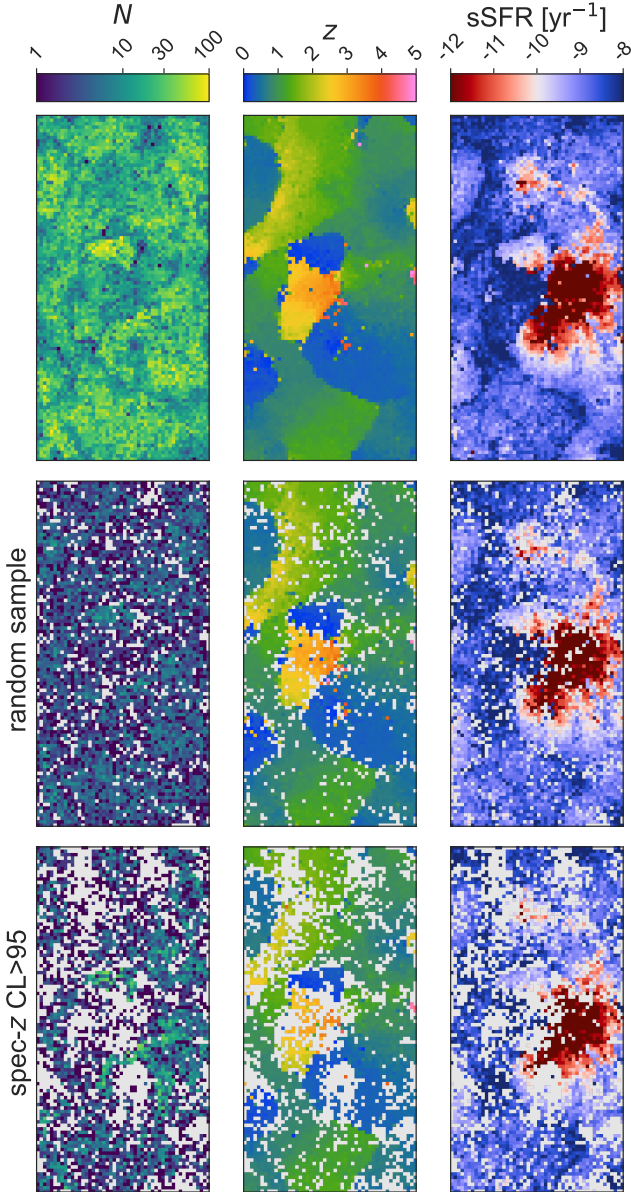


**Figure 2.** A self-organizing map (SOM) partitioning the *ugrizyJH* color space, color-coded by galaxy count (labeled  $N$ ; left column), median redshift ( $z$ ; center column), and median LePHARE specific star formation rate (sSFR; right column). The top row shows the full sample (112,409 sources) with the middle panel color-coded by LePHARE- $z$ . The middle row shows a random sample of photometric objects of the same size as the spec- $z$  sample (14,499 sources) also color-coded by LePHARE- $z$ . The bottom row shows the spec- $z$  CL  $> 95$  sample (14,499 sources), with the spec- $z$  coloring the middle panel. The middle row represents an ideally distributed training data case; it is representative of the full sample and gaps in the coverage of the color space are small and distributed more or less evenly. In contrast, the spectroscopic data (bottom row) illustrates the biased and incomplete coverage of color-redshift space that we aim to mitigate with UMAP-based techniques.

in training redshift in the SOM that cannot be interpolated across.

## 4. REDSHIFT ESTIMATION

### 4.1. Point Estimate Tests

Since our goal is to assess how well redshift can be predicted from position in the SOM or UMAP, we implemented simple algorithms for redshift estimation from each. We then use common photo- $z$  evaluation metrics (see Section 4.2) to quantify the reliability of the color-redshift mapping in these compressed spaces, allowing us to investigate the potential application of UMAP-based methods to optimizing training sets for photo- $z$  algorithms.

For SOM, we used the median of the training redshifts within a cell, hereafter referred to as SOM- $z$ . For UMAP, we instead used the median redshift of the 17 nearest neighbors in the embedding, which we label UMAP- $k$ NN- $z$  (see Appendix C for more details). In each case we used the median rather than the mean due to its robustness to outliers (e.g., incorrect training redshifts); we also tested using the mean instead but obtained worse results. We note that the median  $k$ NN-based interpolation can easily be replaced with a more sophisticated method, as we intend to do in subsequent work.

In one test, we took the sample of 112,409 sources used in generating the embeddings and split it randomly into a training sample of 14,499 sources and a test sample of the remaining 97,910 sources. The redshifts of the test sources were estimated based on the LePHARE- $z$ 's of those in the training sample.

In a second test, we took the 14,499 sources with CL  $> 95$  spec- $z$ 's as the training sample, and estimated the redshifts of a test sample (distinct from that described above but of identical size) consisting of the remaining objects using only these spec- $z$ 's for training. Through these two tests we can compare the utility of SOM- and UMAP-generated embeddings as color-redshift mappings when using representative training data (the random sources with LePHARE- $z$ 's) versus realistically biased spectroscopic training data (the CL  $> 95$  spec- $z$ 's). In both cases, the LePHARE redshifts of the test set are treated as the true values.

When training with the random LePHARE- $z$ 's, roughly 7% of the test sample (6,870 sources) occupied SOM cells that lacked training redshifts, and a redshift estimate could not be assigned. When training with the CL  $> 95$  spec- $z$ 's, this was the case for roughly 23% of the test sample (22,958 sources). UMAP- $k$ NN- $z$  did not face this problem and obtained redshifts for all test sources.

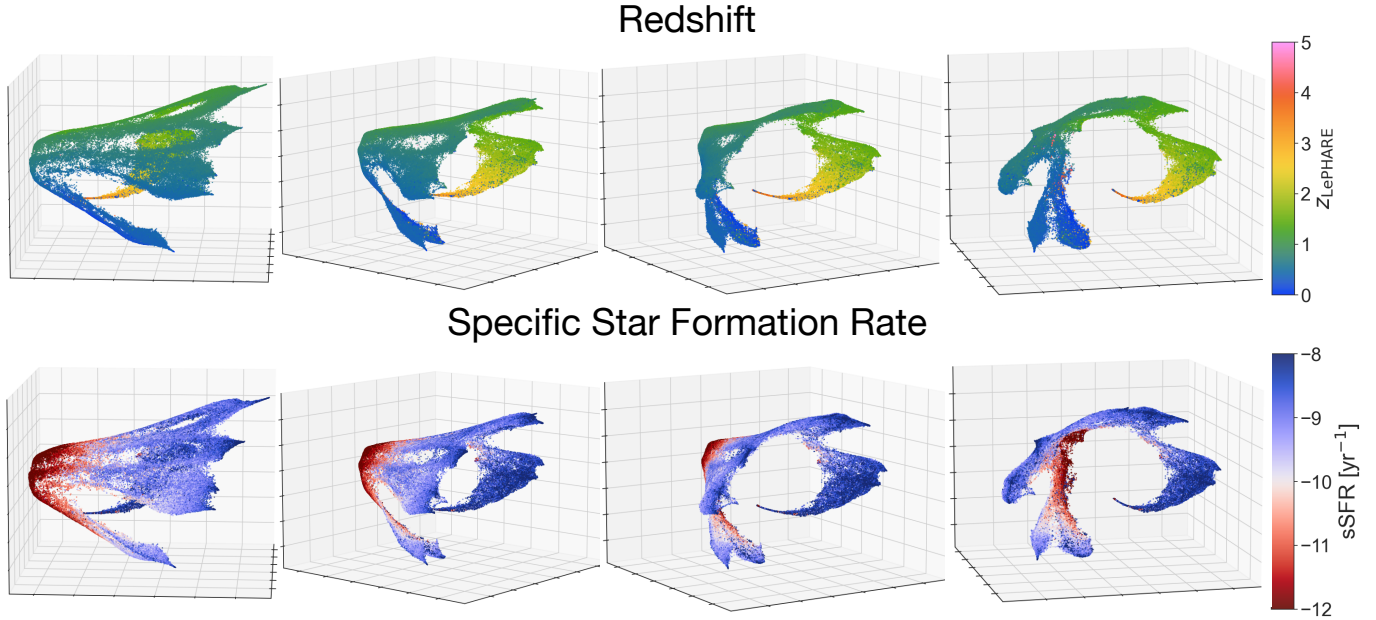


**Figure 3.** A three-dimensional UMAP embedding of the *ugrizyJH* color space for the full sample of 112,409 COSMOS2020 sources. The points are color-coded by LePHARE photo- $z$  (top) and sSFR (bottom). Objects lie on a nearly two-dimensional manifold in this space, exhibiting continuous and monotonic trends in redshift and sSFR in roughly orthogonal directions. This figure shows selected frames from the thirteen-second animation available at <https://finianashmead.github.io/#umap-cosmos2020-video>, in which the plots are rotating about the vertical axes to better illustrate the three-dimensional structure.

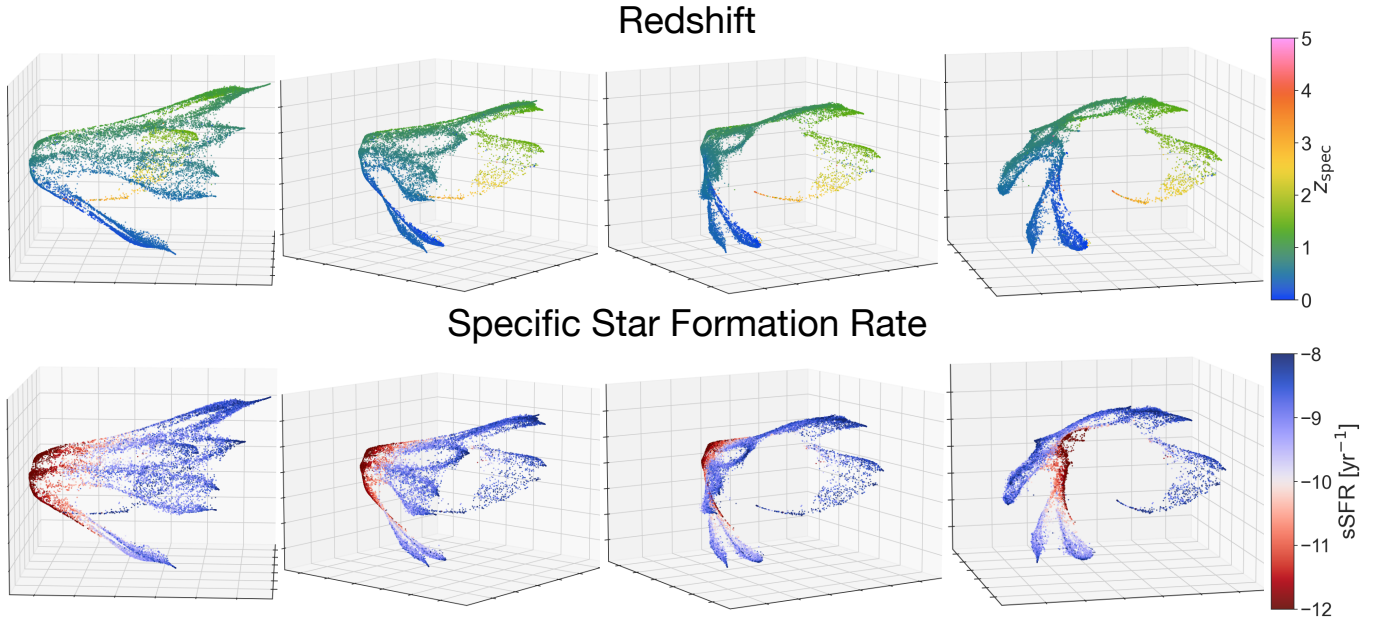


**Figure 4.** A three-dimensional UMAP embedding of the *ugrizyJH* color space showing only the 14,499 sources with high-confidence spec- $z$ 's. The points are color-coded by spec- $z$  (top) and LePHARE sSFR (bottom). Compared to the photometric objects (see Figure 3), the spectroscopic objects provide a more sparse and biased sampling of the manifold. However, unlike the SOM in Figure 2, the trends in redshift and sSFR are continuous across the manifold, enabling accurate interpolation between the spectroscopic objects. This figure shows selected frames from the thirteen-second animation available at <https://finianashmead.github.io/#umap-cosmos2020-video>, in which the plots are rotating about the vertical axes to better illustrate the three-dimensional structure.

#### 4.2. Performance Metrics

We assessed the redshift estimation performance by comparing the predicted redshifts to the **LePHARE** photo- $z$ 's of the test sample, either taken as a whole or when divided into redshift bins of width 0.2 in  $z$ . In the following definitions,  $\Delta z$  indicates the estimated redshift minus the “true” (**LePHARE**) redshift,  $z$ . To evaluate our photo- $z$  point estimate predictions, we used the fraction of outliers, normalized median absolute deviation, and prediction bias:

- **the fraction of outliers** ( $f_{\text{outlier}}$ ), defined as the fraction of predicted photo- $z$ 's for which  $|\frac{\Delta z}{1+z}| > 0.15$ ;
- **the normalized median absolute deviation** ( $\sigma_{\text{NMAD}}$ ), defined as  $1.4826 \times \text{Median}(|\frac{\Delta z}{1+z} - \text{Median}(\frac{\Delta z}{1+z})|)$ ; and
- **the prediction bias**, defined as  $\langle \frac{\Delta z}{1+z} \rangle$ .

In the case of the fraction of outliers, the threshold of 0.15 is commonly used in photo- $z$  validation tests in the literature (e.g., [Hildebrandt et al. 2012](#), [Weaver et al. 2022](#), and [Khostovan et al. 2025](#)). We used  $\sigma_{\text{NMAD}}$  as a robust metric for scatter, which is not affected by outliers so long as they are not too numerous.

#### 4.3. Global Performance

For the SOM, we calculated  $\sigma_{\text{NMAD}}$ ,  $f_{\text{outlier}}$ , and bias values excluding the sources that could not be assigned redshifts, as well as  $f_{\text{outlier}}$  values counting these sources as outliers. Since UMAP- $k\text{NN-}z$  is able to estimate redshifts for all objects while SOM- $z$  is unable to estimate redshifts for objects in cells without training redshifts, we can compare the values of the performance metrics including only the objects in the test sample with SOM- $z$  estimates, in order to evaluate both approaches using an identical test sample.

Overall, we find that using UMAP- $k\text{NN-}z$  results in improved  $f_{\text{outlier}}$  and  $\sigma_{\text{NMAD}}$  in comparison to SOM- $z$ , with the difference in  $f_{\text{outlier}}$  being especially dramatic in the spec- $z$ -trained case. Our results indicate that a UMAP-based approach to dimensionality reduction for mapping the color-redshift relation is particularly advantageous when using sparse or biased training data, as is practically the case with spectroscopic datasets.

When training with the **LePHARE- $z$ 's**, we obtained  $f_{\text{outlier}}$  of 0.0169 using UMAP, 22% lower than the value of 0.0218 obtained using SOM. We obtained a value of 0.0209 for  $\sigma_{\text{NMAD}}$  using UMAP, 13% lower than the 0.0239 obtained with SOM. The bias value was 0.0051 using UMAP, compared to 0.0063 using SOM.

When training with the spec- $z$ 's, using UMAP yielded a 50% lower fraction of outliers, 0.0131 versus 0.0260. UMAP also yielded a  $\sigma_{\text{NMAD}}$  value 11% lower than SOM, with values of 0.0223 and 0.0251, respectively. In this test, the bias values were 0.0020 using UMAP and 0.0024 using SOM.

Test objects assigned to SOM cells without training redshifts comprised  $\sim 7\%$  of the test sample (6,870 objects) when training with the more representative random sample of **LePHARE- $z$ 's**, corresponding to the middle row of Figure 2. When training with the highly-biased sample of high-confidence spec- $z$ 's, corresponding to the bottom row of Figure 2 (in the SOM embedding) or to Figure 4 (in the UMAP embedding),  $\sim 23\%$  of the test objects (22,958 sources) were assigned to SOM cells without training redshifts. As UMAP- $k\text{NN-}z$  is able to estimate redshifts for all of these objects, they can be included in the normal calculation of  $f_{\text{outlier}}$ , while in the case of SOM- $z$  test objects in cells with no training redshifts are counted as outliers. When training with the **LePHARE- $z$ 's**, we obtain  $f_{\text{outlier}}$  of 0.091 for SOM- $z$ , over four times the value of 0.022 for UMAP- $k\text{NN-}z$ . When training with the spec- $z$ 's, we obtain  $f_{\text{outlier}}$  of 0.2544 for SOM- $z$ , more than ten times the value of 0.0242 for UMAP- $k\text{NN-}z$ .

#### 4.4. Performance in Redshift Bins

In Figure 5, we show the trends in  $f_{\text{outlier}}$ ,  $\sigma_{\text{NMAD}}$ , and bias with redshift for SOM and UMAP. The panels on the left show the performance of the SOM- and UMAP-based estimators when training with the representative **LePHARE- $z$ 's**, while the panels on the right show the performance of the estimators when training with the realistically-biased spec- $z$ 's. The exception is the dashed blue line representing the performance of the **LePHARE-trained** UMAP method, which appears on both sides for ease of comparison.

In the **LePHARE-trained** case, the two approaches generally perform similarly when ignoring the sources inhabiting SOM cells without training redshifts, although the  $\sigma_{\text{NMAD}}$  values yielded by the UMAP-based approach remain below those yielded by the SOM-based approach throughout the redshift range. When accounting for the sources inhabiting SOM cells without training redshifts in  $f_{\text{outlier}}$  (the only metric for which this is possible), the UMAP-based method offers much greater reliability at all redshifts.

In the spec- $z$ -trained case, the impact of the spectroscopic data's biased sampling of the color space is clear in the performance of the SOM-based technique. Compared to the **LePHARE-trained** case,  $f_{\text{outlier}}$  (for all cells) increased significantly across the redshift range,



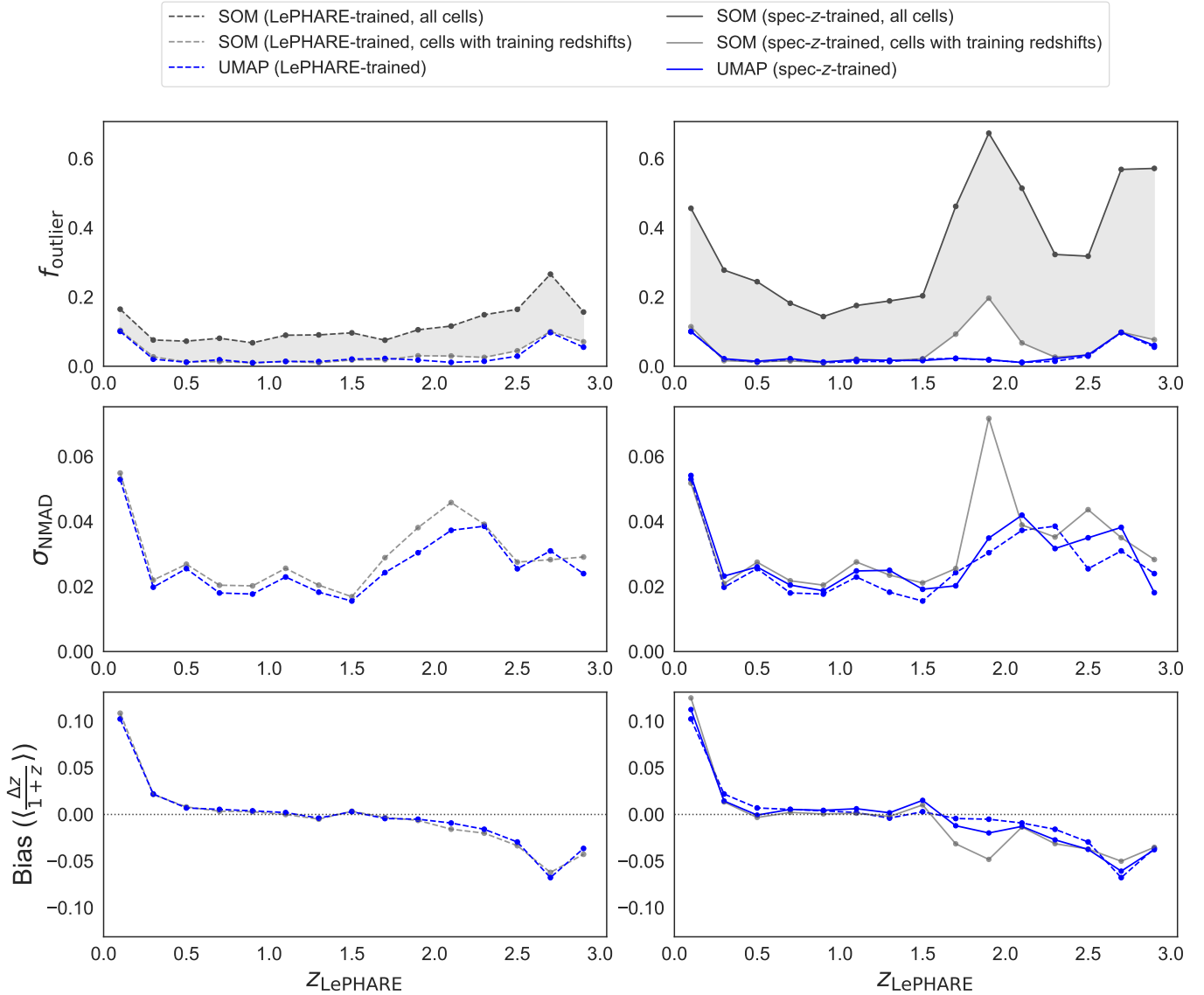


**Figure 5.** Photo- $z$  point estimate metrics  $f_{\text{outlier}}$  (top),  $\sigma_{\text{NMAD}}$  (middle), and bias (bottom) calculated in  $\Delta z = 0.2$  redshift bins for both SOM- $z$  (gray) and UMAP- $k\text{NN-}z$  (blue), when training with a random sample of COSMOS2020 LePHARE photo- $z$ 's (left) and the spec- $z$  CL > 95 sample of spec- $z$ 's (right). For SOM, we compute these metrics (i) only for objects in cells with training data (light gray; i.e. ignoring the regions of color space not represented in the training data) and (ii) assuming that objects in the SOM cells lacking training redshifts are outliers (dark gray; 6,870 sources or 7% of the test sample for LePHARE-trained and 22,958 sources or 23% of the test sample for spec- $z$ -trained). For UMAP, all metrics are computed for the full test samples of 97,910 objects in both training cases. UMAP- $k\text{NN-}z$  yields a lower  $f_{\text{outlier}}$  at all redshifts, especially for the more realistic spec- $z$ -trained case. UMAP- $k\text{NN-}z$  also exhibits lower  $\sigma_{\text{NMAD}}$  and bias across much of the redshift range, quite dramatically in the spec- $z$ -trained case at  $1.8 < z < 2.0$ .

as large numbers of SOM cells inhabited by test objects had no training redshifts. Even ignoring these cells, the impact of the spectroscopic bias in the SOM is clear as a major increase in  $f_{\text{outlier}}$ ,  $\sigma_{\text{NMAD}}$ , and the magnitude of the bias at  $z_{\text{LePHARE}} \sim 1.9$ , where Figure 1 shows a large discrepancy in the normalized density of photometric and spectroscopic sources. The UMAP-based technique, by contrast, is minimally affected by the CSRC data's limited sampling of the color space, as

illustrated in the similarity between the solid and dashed blue curves in the panels in the right column of Figure 5. Furthermore, the spike in  $f_{\text{outlier}}$ ,  $\sigma_{\text{NMAD}}$ , and bias for the SOM-based approach at  $z_{\text{LePHARE}} \sim 1.9$  is completely absent for the UMAP-based approach. This is the key benefit of UMAP's ability to capture the continuous structure of the photometric data driven by underlying physical parameters, such that the redshift of the objects varies smoothly and coherently across the

low-dimensional UMAP embedding and can therefore be interpolated reliably.

Overall, we find the UMAP-based approach to redshift estimation to be highly resilient to biased spectroscopic training data, in stark contrast to the SOM-based approach. As visualized in Figure 2, the discrete nature of the SOM and the discontinuity of the mapping to redshift across SOM cells makes redshift estimation impossible in large regions of the color space when using non-representative training data. With UMAP, however, as visualized in Figure 4, the continuity of the space and the smooth variation in redshift mitigate the issue of the incomplete sampling of the color space by spectroscopic data.

## 5. DISCUSSION

In this work, we found that using UMAP to compress the space of observed galaxy colors has several significant advantages over using a SOM. Due to the discrete nature of the SOM, there is a tradeoff between the resolution with which the color space is represented and the numbers of sources in the cells, with higher cell counts representing the color space in greater detail but with increasingly sparsely populated (or even empty) cells. By projecting each source individually into the output space, UMAP avoids this tradeoff and preserves more information about the structure of the input space.

SOM’s enforced geometry and drive to assign sources to all cells inhibit it from recovering structure occupying a subset of the output space. By contrast, UMAP is able to recover a thin, almost two-dimensional manifold embedded in three-dimensional space. Similarly, UMAP is able to separate low- and high-redshift regions with empty space, while in the SOM projection they can occupy adjacent cells.

Critically, the UMAP embedding exhibits continuous and monotonic trends in redshift and sSFR. This is extremely useful for interpolation across the manifold for redshift prediction, especially for regions with sparse training data. Our results indicate that UMAP dimensionality reduction can recover the simple, intrinsic structure of observed galaxy color space in a way that maps meaningfully to the underlying physical parameters driving it.

The structure of the low-dimensional manifold recovered based on the full photometric sample maps cleanly enough to redshift that UMAP- $k$ NN- $z$  can reliably estimate redshifts based only on a small, highly biased subset of the data. Furthermore, although some detailed structure contained in the higher-dimensional input color space has necessarily been lost or distorted in the compression process,  $k$ NN-based redshift estimation

in the UMAP space yields a lower  $f_{\text{outlier}}$  than that in the seven-dimensional color space in the spec- $z$ -trained case. In the  $z > 1.5$  regime, which is sparsely sampled by the spec- $z$  training data, UMAP yields dramatically better redshift predictions, with 4.4% lower  $\sigma_{\text{NMAD}}$  (0.0328 versus 0.0343), 27% lower  $f_{\text{outlier}}$  (0.0386 versus 0.0526), and 17% lower bias magnitude (-0.0306 versus -0.0368). This is further indication that a UMAP-based approach to mapping color to redshift is particularly advantageous in the case of sparse and highly biased training data.

Interestingly, Dey et al. (2022) recovered UMAP embeddings with key similarities to the one presented in this paper using a very different approach. That investigation used a deep capsule network to compress SDSS  $64 \times 64$ -pixel galaxy postage stamp images in *ugriz* bands ( $64 \times 64 \times 5$  input) into 16-dimensional vectors, which were then further compressed into two- or three-dimensional UMAP embeddings. Similarly to our results, the authors in all cases obtained a curved manifold with a continuous and monotonic redshift sequence. Using Galaxy Zoo spiral/elliptical classifications available for these galaxies, they found morphological trends orthogonal to the trend in redshift. Given the correlation between galaxy morphology and sSFR, this is somewhat analogous to the trend in sSFR being orthogonal to the redshift sequence here. The similarity of our results further indicates that observed high-dimensional photometric galaxy data is largely structured by a small number of physical parameters, and this structure can be studied and leveraged using dimensionality reduction and machine learning.

Going forward, there are several applications of the UMAP-based technique we are exploring. Replacing our initial  $k$ NN-based interpolation with more sophisticated techniques (robust Gaussian process regression) will enable improved redshift estimation and estimation of redshift probability distribution functions and errors at any point in the manifold. Incorporating this, we will be able to interpolate across a UMAP-generated embedding of a photometric sample of galaxy color space populated with spectroscopic sources, and sample from this interpolated manifold to generate representative training data for photo- $z$  algorithms. Likewise, this can be used to identify spectroscopically under-observed regions of color space for prioritization of future observations (e.g. Masters et al. 2015, Khostovan et al. 2025). The embedding can also be populated with mock/simulated galaxies to diagnose differences between their distribution and that of real data, and can similarly be used to improve template-based techniques. Finally, this approach can easily be extended to investigating galaxy properties other than redshift, such as mass-to-light ratio, stel-

lar mass, and sSFR. We provide the necessary Python code to reproduce all figures and animations at [https://github.com/finianashmead/UMAP\\_COSMOS2020/](https://github.com/finianashmead/UMAP_COSMOS2020/).

## ACKNOWLEDGMENTS

F. A., J. A. N., and B. H. A. acknowledge the support of the National Aeronautics and Space Administration under grant No. 80NSSC24K0083.

B.D. is a postdoctoral fellow at the University of Toronto in the Eric and Wendy Schmidt AI in Science Postdoctoral Fellowship Program, a program of Schmidt Sciences.

The presentation of this work was influenced by valuable conversations with colleagues at the University of Pittsburgh and other institutions, including Joel Leja,

Joshua Speagle, Tianqing Zhang, Ashod Khederlarian, Yoquelbin Salcedo Hernandez, and Federico Berlfein. We would also like to thank the Survey Science group at the Kavli Institute for Cosmological Physics at the University of Chicago and its co-leader Chihway Chang, who hosted the author to present early results during the writing of this paper and offered valuable feedback and lines of questioning.

*Software:* `astropy` (Astropy Collaboration et al. 2022), `matplotlib` (Hunter 2007), `minisom` (Vettigli 2018), `numpy` (Harris et al. 2020), `pandas` (Wes McKinney 2010; pandas development team 2020), `scikit-learn` (Pedregosa et al. 2011), `scipy` (Virtanen et al. 2020), `seaborn` (Waskom 2021), `umap-learn` (McInnes et al. 2018)

## APPENDIX

### A. SOM OPTIMIZATION

We generated SOM embeddings with a  $1 \times 2$  aspect ratio consisting of rectangular cells, as in, e.g., Masters et al. (2015). Specifically, we tested maps of dimensions (8, 16); (12, 24); (18, 36); (25, 50); (35, 70); (50, 100); and (75, 150). These size intervals were chosen such that the total cell number roughly doubles with each increase. In all cases, we used the default values of the SOM sigma and learning rate hyperparameters of 1 and 0.5, respectively, and two million training epochs. Weighing the advantage of capturing detailed structure against the disadvantages of sparsely populated cells, we selected the (50, 100) SOM as the best option.

At the lower cell counts, there are few to no cells unoccupied by photometric objects, and few objects in cells without training redshifts in either the LePHARE-trained or spec-z-trained case. For instance, in the  $8 \times 16$  SOM, zero cells are not occupied by any photometric objects, and only 29 and 261 test objects, respectively, occupied SOM cells with no training redshifts in the LePHARE-trained and spec-z-trained cases. However, the low resolution of this representation of the color space leads to high  $\sigma_{\text{NMAD}}$  values in comparison to the SOM we use in the main paper, 0.0359 versus 0.0239 and 0.0396 versus 0.0251 for the LePHARE-trained and spec-z-trained cases, respectively. Likewise, the values of  $f_{\text{outlier}}$  for test objects assigned redshifts are higher than those we obtain in the main paper, 0.0318 versus 0.0218 and 0.0418 versus 0.026 for the respective training cases. At the high end of the cell counts,  $75 \times 150$ , the structure of the color space is captured in greater detail, but larger regions of the SOM are sparsely populated or contain no training redshifts. This results in slightly lower  $\sigma_{\text{NMAD}}$  values, 0.0237 and 0.0241, respectively, as well as a slightly lower  $f_{\text{outlier}}$  value in the spec-z-trained case, 0.0238. However, in this SOM the sparse population of cells becomes particularly problematic, as 44 cells contain no photometric objects, and 25,818 and 43,706 test objects occupy cells without training redshifts in the LePHARE-trained and spec-z-trained cases, respectively. In the spec-z-trained case, the value of  $f_{\text{outlier}}$  including objects in cells without training redshifts is 46%.

While the  $50 \times 100$  SOM struck the best balance between resolution of the color space and occupation of cells, a handful of unoccupied cells were present. We tested adjusting the SOM hyperparameters as well as the number of training epochs, including sigma values between 1 and 10, learning rate values between 0.5 and 0.9, and numbers of training epochs between two million and five million. We selected the SOM generated using sigma of 1, learning rate of 0.8, and two million training epochs as it was the only version we tested with all cells inhabited by objects in our photometric sample.

### B. UMAP OPTIMIZATION

We generated UMAP embeddings in two and three dimensions for a range of hyperparameters and data pre-processing steps, using the `umap-learn` Python package. Other than the dimensionality of the UMAP embedding and the key hyperparameters `min.dist` and `n.neighbors`, these options include rescaling the input data and using the densMAP

version of UMAP (Narayan et al. 2020). While UMAP normally assumes the existence of a manifold on which the data is uniformly distributed, the densMAP version aims to preserve variations in local density of the input data. This version was used in Dey et al. (2022).

Through a qualitative visual analysis, we looked for smoothness of the trend in redshift and spatial separation of the low- and high-redshift ends of the manifold. In this way we determined that the best results were obtained using three-dimensional UMAP embeddings generated from non-rescaled data, without using densMAP, using the Manhattan distance metric in the input space, and setting the `min_dist` hyperparameter to 0.00. We tested values of `min_dist` from 0.00 to 0.20, finding that 0.00 was the only value that yielded embeddings without filamentary structure connecting the low- $z$  and high- $z$  ends of the manifold. We tested values of `n_neighbors` from 10 to 200, recovering qualitatively identical embeddings for values between 55 and 85.

At this stage, we implemented a quantitative analysis of the embeddings, selecting the version in which our photo- $z$  evaluation metrics described in Section 4.2 were minimized, with the highest priority given to  $f_{\text{outlier}}$  in the spec- $z$ -trained case. Through this analysis, we determined that the best embedding for mapping color to redshift was obtained with `n_neighbors=80`.

Rescaling of input data to have similar dynamic range in all dimensions is a common pre-processing step in machine learning and dimensionality reduction problems, however in this case our results seem to indicate that differences in the dynamic ranges of photometric colors contain useful information.

### C. UMAP- $k$ NN- $z$ AND SOM- $z$ CALCULATION

For UMAP- $k$ NN- $z$ , we tested three different methods of redshift estimation; mean redshift, inverse-distance-weighted mean redshift, and median redshift of the  $k$  nearest neighbors. We also tested a range of values for  $k$  from 5 to 41. Here we report the photo- $z$  performance metrics for the spec- $z$ -trained case of the redshift interpolation test.

In the case of the mean and the inverse-distance-weighted mean, the  $\sigma_{\text{NMAD}}$  values were best at 19 and 21 neighbors with values of 0.0281 and 0.0277, respectively, increasing with lower or higher  $k$  values. Conversely,  $f_{\text{outlier}}$  values for the mean and inverse-distance-weighted-mean decrease monotonically with increasing  $k$ , reaching best values of 0.0302 and 0.0312, respectively, at  $k = 41$ . At this  $k$ , their respective  $\sigma_{\text{NMAD}}$  values reached 0.0288 and 0.028.

The best performance was achieved using the median redshift of the  $k$  nearest neighbors. For this estimator, the value of  $f_{\text{outlier}}$  was less dependent on  $k$  than when a mean was used. The best  $\sigma_{\text{NMAD}}$  value was 0.0249, achieved at 11 neighbors (at which  $f_{\text{outlier}} = 0.025$ ), while the best  $f_{\text{outlier}}$  value was 0.0239, achieved at 25 neighbors (at which  $\sigma_{\text{NMAD}} = 0.0252$ ). Both metrics increase as  $k$  deviates from these values, but the effect is relatively minor, especially in the direction of increasing  $k$ , as the median redshift of any object's  $k$  nearest neighbors in the UMAP embedding is unlikely to change when considering increasingly distant neighbors due to the coherence of the redshift sequence. Balancing consideration of  $\sigma_{\text{NMAD}}$  and  $f_{\text{outlier}}$ , we selected median-based redshift estimation with  $k = 17$ , yielding  $\sigma_{\text{NMAD}} = 0.025$  and  $f_{\text{outlier}} = 0.0242$ .

In the case of SOM- $z$ , we could use the mean or the median of the training redshifts in each cell as a similarly simple redshift point estimate. In all SOM sizes we tested, the median performed better than the mean on all metrics. For the  $50 \times 100$  SOM projection used in the main paper, the  $f_{\text{outlier}}$ ,  $\sigma_{\text{NMAD}}$ , and bias values for the spec- $z$ -trained case using the mean cell redshifts were 0.028, 0.0258, and 0.0017, respectively, versus 0.026, 0.0251, and 0.0024.

### REFERENCES

- |   |  |
|---|--|
| <p>Aihara, H., AlSayyad, Y., Ando, M., et al. 2019, PASJ, 71, 114, doi: <a href="https://doi.org/10.1093/pasj/psz103">10.1093/pasj/psz103</a></p> <p>Arnouts, S., Cristiani, S., Moscardini, L., et al. 1999, MNRAS, 310, 540, doi: <a href="https://doi.org/10.1046/j.1365-8711.1999.02978.x">10.1046/j.1365-8711.1999.02978.x</a></p> <p>Astropy Collaboration, Price-Whelan, A. M., Lim, P. L., et al. 2022, ApJ, 935, 167, doi: <a href="https://doi.org/10.3847/1538-4357/ac7c74">10.3847/1538-4357/ac7c74</a></p> <p>Blanquez, D., Davidzon, I., &amp; Magdis, G. 2023, Notebook to analyse the COSMOS2020 catalogue, <a href="https://github.com/cosmic-dawn/cosmos2020-readcat">https://github.com/cosmic-dawn/cosmos2020-readcat</a></p> | <p>Brammer, G. B., van Dokkum, P. G., &amp; Coppi, P. 2008, ApJ, 686, 1503, doi: <a href="https://doi.org/10.1086/591786">10.1086/591786</a></p> <p>Carrasco Kind, M., &amp; Brunner, R. J. 2014, MNRAS, 438, 3409, doi: <a href="https://doi.org/10.1093/mnras/stt2456">10.1093/mnras/stt2456</a></p> <p>Dey, B., Andrews, B. H., Newman, J. A., et al. 2022, MNRAS, 515, 5285, doi: <a href="https://doi.org/10.1093/mnras/stac2105">10.1093/mnras/stac2105</a></p> <p>Harris, C. R., Millman, K. J., van der Walt, S. J., et al. 2020, Nature, 585, 357, doi: <a href="https://doi.org/10.1038/s41586-020-2649-2">10.1038/s41586-020-2649-2</a></p> <p>Hemmati, S., Capak, P., Pourrahmani, M., et al. 2019, ApJL, 881, L14, doi: <a href="https://doi.org/10.3847/2041-8213/ab3418">10.3847/2041-8213/ab3418</a></p> |
|---|--|



- Hildebrandt, H., Erben, T., Kuijken, K., et al. 2012, MNRAS, 421, 2355, doi: [10.1111/j.1365-2966.2012.20468.x](https://doi.org/10.1111/j.1365-2966.2012.20468.x)
- Hunter, J. D. 2007, Computing in Science & Engineering, 9, 90, doi: [10.1109/MCSE.2007.55](https://doi.org/10.1109/MCSE.2007.55)
- Ilbert, O., Arnouts, S., McCracken, H. J., et al. 2006, A&A, 457, 841, doi: [10.1051/0004-6361:20065138](https://doi.org/10.1051/0004-6361:20065138)
- Ilbert, O., McCracken, H. J., Le Fèvre, O., et al. 2013, A&A, 556, A55, doi: [10.1051/0004-6361/201321100](https://doi.org/10.1051/0004-6361/201321100)
- Khostovan, A. A., Kartaltepe, J. S., Salvato, M., et al. 2025, arXiv e-prints, arXiv:2503.00120, doi: [10.48550/arXiv.2503.00120](https://doi.org/10.48550/arXiv.2503.00120)
- Kohonen, T. 1982, Biol. Cybern. 43, 59. <https://doi.org/10.1007/BF00337288>
- Mandelbaum, R. 2018, ARA&A, 56, 393, doi: [10.1146/annurev-astro-081817-051928](https://doi.org/10.1146/annurev-astro-081817-051928)
- Masters, D., Capak, P., Stern, D., et al. 2015, ApJ, 813, 53, doi: [10.1088/0004-637X/813/1/53](https://doi.org/10.1088/0004-637X/813/1/53)
- McCracken, H. J., Milvang-Jensen, B., Dunlop, J., et al. 2012, A&A, 544, A156, doi: [10.1051/0004-6361/201219507](https://doi.org/10.1051/0004-6361/201219507)
- McCullough, J., Gruen, D., Amon, A., et al. 2024, MNRAS, 531, 2582, doi: [10.1093/mnras/stae1316](https://doi.org/10.1093/mnras/stae1316)
- McInnes, L., Healy, J., Saul, N., & Großberger, L. 2018, Journal of Open Source Software, 3, 861, doi: [10.21105/joss.00861](https://doi.org/10.21105/joss.00861)
- Narayan, A., Berger, B., & Cho, H. 2020, bioRxiv, doi: [10.1101/2020.05.12.077776](https://doi.org/10.1101/2020.05.12.077776)
- Newman, J. A., & Gruen, D. 2022, ARA&A, 60, 363, doi: [10.1146/annurev-astro-032122-014611](https://doi.org/10.1146/annurev-astro-032122-014611)
- pandas development team, T. 2020, pandas-dev/pandas: Pandas, latest, Zenodo, doi: [10.5281/zenodo.3509134](https://doi.org/10.5281/zenodo.3509134)
- Pedregosa, F., Varoquaux, G., Gramfort, A., et al. 2011, Journal of Machine Learning Research, 12, 2825
- Salvato, M., Ilbert, O., & Hoyle, B. 2019, Nature Astronomy, 3, 212, doi: [10.1038/s41550-018-0478-0](https://doi.org/10.1038/s41550-018-0478-0)
- Sawicki, M., Arnouts, S., Huang, J., et al. 2019, MNRAS, 489, 5202, doi: [10.1093/mnras/stz2522](https://doi.org/10.1093/mnras/stz2522)
- Schlegel, D. J., Finkbeiner, D. P., & Davis, M. 1998, ApJ, 500, 525, doi: [10.1086/305772](https://doi.org/10.1086/305772)
- The LSST Dark Energy Science Collaboration, Mandelbaum, R., Eifler, T., et al. 2018, arXiv e-prints, arXiv:1809.01669, doi: [10.48550/arXiv.1809.01669](https://doi.org/10.48550/arXiv.1809.01669)
- Vettigli, G. 2018, MiniSom: minimalistic and NumPy-based implementation of the Self Organizing Map. <https://github.com/JustGlowing/minisom/>
- Virtanen, P., Gommers, R., Oliphant, T. E., et al. 2020, Nature Methods, 17, 261, doi: [10.1038/s41592-019-0686-2](https://doi.org/10.1038/s41592-019-0686-2)
- Waskom, M. 2021, The Journal of Open Source Software, 6, 3021, doi: [10.21105/joss.03021](https://doi.org/10.21105/joss.03021)
- Weaver, J. R., Kauffmann, O. B., Ilbert, O., et al. 2022, ApJS, 258, 11, doi: [10.3847/1538-4365/ac3078](https://doi.org/10.3847/1538-4365/ac3078)
- Wes McKinney. 2010, in Proceedings of the 9th Python in Science Conference, ed. Stéfan van der Walt & Jarrod Millman, 56 – 61, doi: [10.25080/Majora-92bf1922-00a](https://doi.org/10.25080/Majora-92bf1922-00a)
- Zasowski, G., Jha, S. W., Chomiuk, L., et al. 2025, arXiv e-prints, arXiv:2505.10574, doi: [10.48550/arXiv.2505.10574](https://doi.org/10.48550/arXiv.2505.10574)